Micromechanical analysis on the influence of the Lode parameter on void growth and coalescence

Imad Barsoum [a,*], Jonas Faleskog [b]

[a] Department of Mechanical Engineering, The Petroleum Institute, P.O. Box 2533, Abu Dhabi, United Arab Emirates
[b] Department of Solid Mechanics, Royal Institute of Technology, SE-100 44 Stockholm, Sweden

ABSTRACT

A micromechanical model consisting of a band with a square array of equally sized cells, with a spherical void located in each cell, is developed. The band is allowed a certain inclination and the periodic arrangement of the cells allow the study of a single unit cell for which fully periodic boundary conditions are applied. The model is based on the theoretical framework of plastic localization and is in essence the micromechanical model by Barsoum and Faleskog (Barsoum, I., Faleskog, J., 2007. Rupture mechanisms in combined tension and shear—micromechanics. International Journal of Solids and Structures 44(17), 5481–5498) with the extension accounting for the band orientation. The effect of band inclination is significant on the strain to localization and cannot be disregarded. The macroscopic stress state is characterized by the stress triaxiality and the Lode parameter. The model is used to investigate the influence of the stress state on void growth and coalescence. It is found that the Lode parameter exerts a strong influence on the void shape evolution and void growth rate as well as the localized deformation behavior. At high stress triaxiality level the influence of the Lode parameter is not as marked and the overall ductility is set by the stress triaxiality. For a dominating shear stress state localization into a band cannot be regarded as a void coalescence criterion predicting material failure. A coalescence criterion operative at dominating shear stress state is needed.

© 2010 Elsevier Ltd. All rights reserved.

1. Introduction

It is a well known fact that the stress triaxiality has a significant influence on void growth and coalescence and hence on the ductility of materials. This has been demonstrated by several authors in the past, both experimentally, theoretically and numerically. The classical work by Hancock and Mackenzie (1976), where they perform experiments on notched round bar specimens, show that ductility increases with decreasing stress triaxiality. These experimental findings are annotated by the use of the theoretical void growth models by McClintock (1968) and Rice and Tracey (1969). Recently, Weck et al. (2006) perform an experimental study on void coalescence in voided layers and observe that the voids grow until a critical spacing between them is reached, which corresponds to the onset of coalescence. Beyond this point two different ductile failure mechanisms leading to final rupture are observed. One is void shearing due to that the deformation becomes concentrated into a narrow shear band between the larger voids leading to micro-void nucleation at second phase particles (Cox and Low, 1974; Faleskog and Shih, 1997). The other mechanism is referred

to as void coalescence by internal necking, where the ligament between the voids necks down to a point. This event is studied extensively numerically e.g. by Koplik and Needleman (1988), Pardoen and Hutchinson (2000) and most recently by Scheyvaerts et al. (2010), who investigate the influence of the stress triaxiality on void growth and coalescence under axisymmetric conditions by the use of a cell model. However, it has been observed in recent experimental studies by Wierzbicki et al. (2005) and Barsoum and Faleskog (2007a) that the stress triaxiality is insufficient to characterize the stress state in ductile failure. A deviatoric stress measure is also needed and the stress state is hence characterized by the stress triaxiality and the Lode parameter.

Zhang et al. (2001) and Gao and Kim (2006) perform systematic numerical analysis on a cell model with straight boundaries subjected to different macroscopic stress states characterized by the Lode parameter and stress triaxiality. They find that the Lode parameter has a strong influence on the stress carrying capacity of the material and the onset of void coalescence, which they define as the shift to an uniaxial straining mode. As a consequence of the constraint on the cell not allowing for shear deformation, the uniaxial straining mode is the only mode of localization that will occur in their model. Other cell studies by Tvergaard (1981), Tvergaard (1982), Pijnenburg and Van der Giessen (2001) and

* Corresponding author. Tel.: +971 2 6075273; fax: +971 2 6075194.
  E-mail address: ibarsoum@pi.ac.ae (I. Barsoum).

Leblond and Mottet (2008) incorporate the possibility of shear deformation by employing fully periodic boundary conditions, but they do not systematically investigate the effect of the Lode parameter.

In a recent study, Barsoum and Faleskog (2007b) employ a micromechanical model to study the ductile rupture mechanisms observed in their experimental investigation on double notched tube specimens subjected to combined tension and torsion (Barsoum and Faleskog, 2007a). The micromechanical model assumes that ductile failure is a consequence of that plastic deformation localizes into a band and is based on the model introduced by Rudnicki and Rice (1975) and Rice (1977). The model consists of a planar band with a square array of equally sized cells, with an initially spherical void in the center of each cell. The periodic arrangement of cells allows for the study of a single unit cell for which fully periodic boundary conditions are applied within the band. The loading condition of the unit cell is chosen such that it resembles the stress state, characterized by the stress triaxiality and the Lode parameter of the experiments. The model captures the experimental trend fairly well and predicts the different rupture mechanisms involved but does not account for the orientation of the band, which has an important role in the localization behavior. Tvergaard (2009b), Tvergaard (2009a) has very recently carried out a series of similar micromechanical studies, where a combination of normal stress and shear stress is applied to unit cells under plane strain conditions. Tvergaard's results demonstrates that voids deforming under zero or low stress triaxiality may lead to material softening. Also Scheyvaerts et al. (in press) have most recently studied material softening and failure due to growth and coalescence of voids under combined tension and shear. However, both Tvergaard (2009b), Tvergaard (2009a) and Scheyvaerts et al. (in press) use a similar model as in Barsoum and Faleskog (2007b), and do not fully account for the influence of the orientation of the voided cells.

The influence of the band orientation on the localization behavior has been the subject of studies in the past. Yamamoto (1978) adopts elastic–plastic constitutive relations for a void-containing material to develop a criterion for localization under plane strain conditions. The same procedure is employed by Saje et al. (1982) where they investigate the influence of void nucleation and band orientation on localization under plane strain and axisymmetric conditions. Tvergaard (1989) uses a two dimensional computational cell model and employs fully periodic boundary conditions to incorporate the possibility of shear deformation to study the influence of band orientation. They all find that the orientation of the band has a significant influence on localization. Nahshon and Hutchinson (2008) propose a modified Gurson model to account for shear failure. They perform a localization analysis, following earlier localization studies employed by Mear and Hutchinson (1985), where they explore the relationship of the localization strain to the Lode parameter, stress triaxiality and band orientation.

In the current study the micromechanical model in Barsoum and Faleskog (2007b) is extended to incorporate the effect of band orientation in a somewhat simplified manner. The objective is to explore the influence of the Lode parameter and the band orientation on the localization behavior, void growth and coalescence. The model is presented in Section 2, the mechanical properties of the materials considered are summarized in Section 3 and the results of the micromechanical analysis are presented in Sections 4 and 5. The paper is concluded in Section 6.

2. Micromechanical model

Building on the work by Marciniak and Kuczynski (1967), Rudnicki and Rice (1975) and Rice (1977) investigate the condi-

tions corresponding to localization of deformation into a planar band and present a general framework for imperfection based localization analysis, as is also discussed by Needleman and Tvergaard (1992). The present micromechanical analysis fits well into the theoretical framework given by Rudnicki and Rice (1975). The micromechanical model employed here assumes that ductile material failure occurs when the deformation becomes highly non-uniform and localizes into a thin planar band as a result of nucleation, growth and coalescence of voids. The material is assumed to contain an initial planar band with a regular square array of pre-existing voids that can be viewed as initial imperfections, which may induce localization of deformation. Thus the stage of void nucleation is not considered in the present study.

A systematic study of the influence of the full range of the Lode parameter, L $(-1 \leqslant L \leqslant 1)$, on void growth and coalescence can be done in several ways. As in Barsoum and Faleskog (2007b) we consider a material subjected to a combination of an axisymmetric and a pure shear stress state, as shown in Fig. 1(a) with reference to the Cartesian coordinate system $X_1^0 X_2^0 X_3^0$. Localization into a planar band, as shown in Fig. 1(b), may then occur in a symmetric mode, a shear mode or a combination of both modes. In general, the band will localize in the most favorable direction and thus the orientation of the band should be considered. The orientation of the band is here defined by θ, the angle between the band and the macroscopic Cauchy stress component Σ_{33}^0 along the X_3^0-axis, according to Fig. 1(a). As shown by Rudnicki and Rice (1975) and further discussed by Perrin and Leblond (1993), the normal to the plane of localization will always be perpendicular to the direction of the middle principal stress $\Sigma_{II} = \Sigma_{22}^0$ and located in the $X_1^0 - X_3^0$ plane. Hence, the unit normal vector of the band is taken to be in the $X_1^0 - X_3^0$ plane and perpendicular to the X_2^0-axis. At this point we introduce a second Cartesian coordinate system $X_1 X_2 X_3$, rotated an angle θ such that X_1 is normal to the band in Fig. 1(c) and (d) with $X_2 = X_2^0$, as shown in Fig. 1. The macroscopic stress components Σ_{ij} with reference to $X_1 X_2 X_3$ acting on the inclined band in Fig. 1(c) can readily be obtained by tensorial transformation of the macroscopic stress components Σ_{ij}^0 in Fig. 1(b). As discussed above, the maximum and minimum principal stresses, Σ_I and Σ_{III}, respectively, are located in the $X_1^0 - X_3^0$. Their directions are here defined by the angle α between Σ_{III} and the X_3^0-axis. For later purposes we introduce the angle $\varphi = \theta + \alpha$ and note that $\Sigma_I \geqslant \Sigma_{II} = \Sigma_{22}^0 \geqslant \Sigma_{III}$, see Fig. 1(d).

The influence of the band orientation is accounted for in a simplified manner in this study. Upon deformation the orientation of the inclined band in Fig. 1(a) will change such that the angle between X_3^0-axis and the band evolves as $\tan\theta_{def} = (F_{13} + F_{11}\tan\theta)/(F_{33} + F_{31}\tan\theta)$, where θ_{def} is the angle in the deformed configuration and F_{ij} are components of the deformation gradient with reference to the Cartesian frame $(X_1^0 X_2^0 X_3^0)$. Here, we do not account for the evolution of the angle with deformation. Instead, given a fixed set of the stress triaxiality and the Lode parameter, we apply proportional stressing on the aggregate of cells in the inclined plane in Fig. 1(c) and seek the angle θ that minimizes the strain to failure. Hence, the angle θ shown in Fig. 1(a) may be viewed as the angle at the instance of localization. Put in an another way, the stress state in Fig. 1(c) is co-rotating with the inclined band during deformation and thus the coordinate system $X_1 X_2 X_3$ is used as the reference system. In this way, we can fully employ the micromechanical model developed in Barsoum and Faleskog (2007b) in which the periodic boundary conditions are formulated based on the assumption of proportional stressing. Note that for the special case of no initial band inclination, the band will not rotate during deformation. This special case is also considered below.

Due to the regular array of voids, attention can be restricted to a three dimensional unit cell as indicated in Fig. 1(e), with dimensions $2D_1$, D_2 and D_3. The height of the unit cell ($2D_1$) is taken large
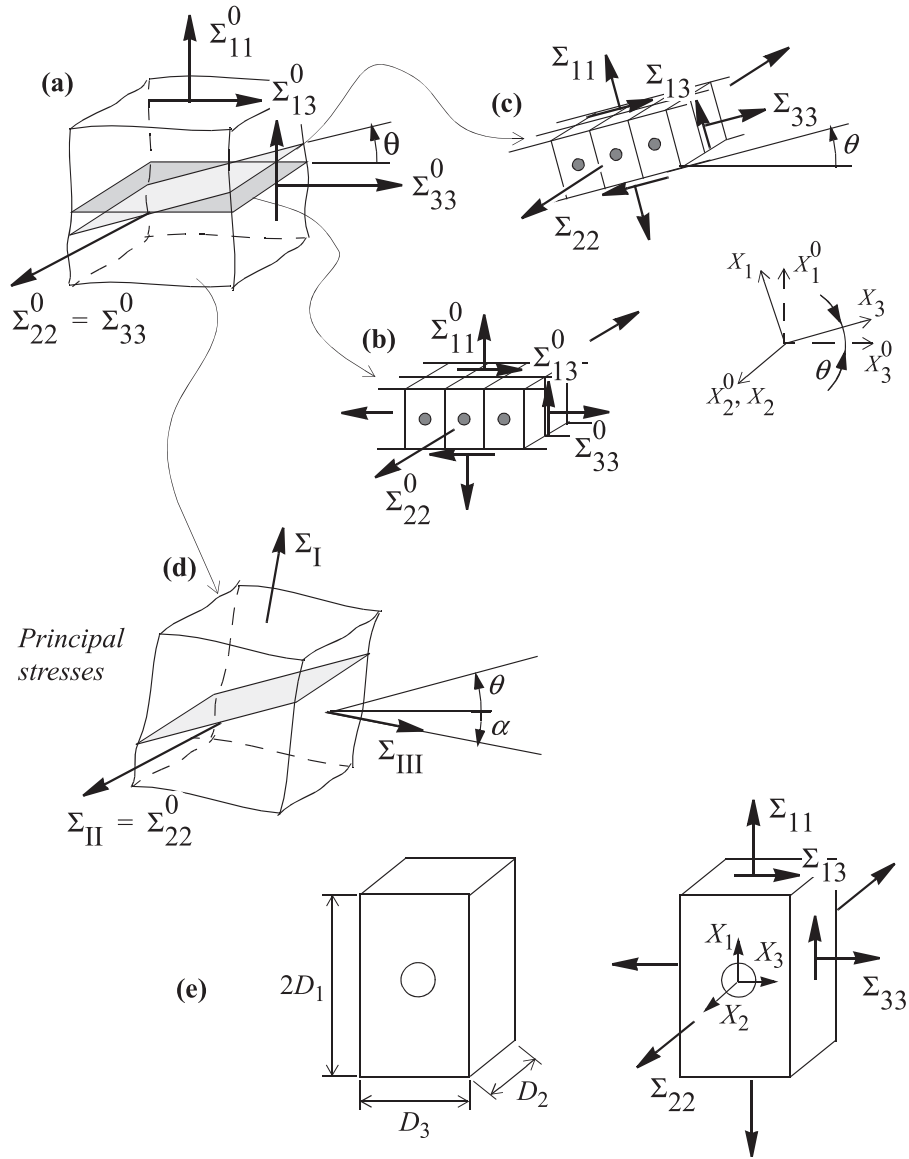
Fig. 1. The micromechanical model: (a) material subjected to a combination of axisymmetric and pure shear stress state indicating two bands with (b) macroscopic stresses Σ_{ij}^0 acting on a planar band containing pre-existing spherical voids. (c) The inclined band depicted in the principal stress space with (d) macroscopic stresses Σ_{ij} acting on the inclined band with inclination angle θ. (e) Dimensions of the unit cell and macroscopic stresses acting on the unit cell referring to a Cartesian coordinate system with origin at the center of the void.

enough to avoid interaction with other rows of voids. The influence of the height of the unit cell can be quantitatively appreciated from Pardoen and Hutchinson (2000). The unit cell contains one void placed in its center, initially of spherical shape with radius R_0. The initial size of the cell is given by $D_1 = D_2 = D_3 = D_0$. The initial ratio of void size to void spacing is defined as $\chi_0 = R_0/D_0$ and the initial void volume fraction is $f_0 = \chi_0^3 \pi/12$, where χ_0 is the more relevant parameter for defining porosity in the present study.

2.1. Loading of the 3D unit cell

The macroscopic Cauchy stresses Σ_{ij}^0 acting on the unit cell, in the band shown in Fig. 1(b), are equal to the volume average of the Cauchy stresses, σ_{ij}^0, over the deformed volume of the unit cell V, and can be calculated as

$$\Sigma_{ij}^0 = \frac{1}{V} \int_V \sigma_{ij}^0 \, dV. \tag{1}$$

The mean value and the von Mises effective value of the macroscopic stress are then defined as

$$\Sigma_h = \frac{1}{3} \left(\Sigma_{11}^0 + \Sigma_{22}^0 + \Sigma_{33}^0 \right), \tag{2}$$

$$\Sigma_e = \frac{1}{\sqrt{2}} \sqrt{ \left(\Sigma_{11}^0 - \Sigma_{22}^0 \right)^2 + \left(\Sigma_{22}^0 - \Sigma_{33}^0 \right)^2 + \left(\Sigma_{33}^0 - \Sigma_{11}^0 \right)^2 + 6 \left(\Sigma_{13}^0 \right)^2 }. \tag{3}$$

Loading is applied on the unit cell such that the macroscopic stresses acting on the cell follow a proportional loading history defined by the stress ratios

$$\Sigma_{22}^0/\Sigma_{11}^0 = \Sigma_{33}^0/\Sigma_{11}^0 = \rho_n, \quad \Sigma_{13}^0/\Sigma_{11}^0 = \rho_s, \tag{4}$$

where ρ_n and ρ_s are prescribed constants corresponding to normal and shear stress ratios, respectively. The remaining shear stress components, Σ_{12}^0 and Σ_{23}^0, are equal to zero. By varying ρ_n and ρ_s a combination of axisymmetric and pure shear stress states can be accomplished. The stress invariants, the stress triaxiality T and the Lode parameter L, will then remain constant during the load history as

$$T = \frac{\Sigma_h}{\Sigma_e} = \frac{(1 + 2\rho_n) \cdot \text{sign}(\Sigma_{11}^0)}{3\sqrt{(1 - \rho_n)^2 + 3\rho_s^2}}, \tag{5}$$

$$L = \frac{2\Sigma_{\text{II}} - \Sigma_{\text{I}} - \Sigma_{\text{III}}}{\Sigma_{\text{I}} - \Sigma_{\text{III}}} = -\frac{(1 - \rho_n) \cdot \text{sign}(\Sigma_{11}^0)}{\sqrt{(1 - \rho_n)^2 + 4\rho_s^2}}, \tag{6}$$

where $\Sigma_{\text{I}} \geqslant \Sigma_{\text{II}} = \Sigma_{22}^0 \geqslant \Sigma_{\text{III}}$ are the principal stresses as illustrated in Fig. 1(d). The inverse relations from Eqs. (5) and (6), the stress ratios ρ_n and ρ_s can be expressed as

$$\rho_n = \frac{3T\sqrt{3 + L^2} + 2L}{3T\sqrt{3 + L^2} - 4L}, \quad \rho_s = \frac{3\sqrt{1 - L^2}}{3T\sqrt{3 + L^2} - 4L}. \tag{7}$$

The solutions for ρ_n and ρ_s are valid for $-1 \leqslant L \leqslant 1$ and $\Sigma_{11} \geqslant 0$ when $T \gtrsim 4L/(3\sqrt{3 + L^2})$. A few limiting cases are here of interest. These are: $\rho_n = -1/2$ and $\rho_s = -3\sqrt{1 - L^2}/(4L)$ for $T \to 0$; $\rho_n = 1$ and $\rho_s = 1/(\sqrt{3}T)$ for $L \to 0$; $\rho_n = (3T \pm 1)/(3T \mp 2)$ and $\rho_s = 0$ for $L \to \pm 1$.

The macroscopic principal stresses are given by

$$\begin{aligned}
\Sigma_{\text{I}} &= \frac{1}{2}\left(1 + \rho_n + \sqrt{(1 - \rho_n)^2 + 4\rho_s^2}\right)\Sigma_{11}^0, \\
\Sigma_{\text{II}} &= \Sigma_{22}^0 = \rho_n\Sigma_{11}^0 \\
\Sigma_{\text{III}} &= \frac{1}{2}\left(1 + \rho_n - \sqrt{(1 - \rho_n)^2 + 4\rho_s^2}\right)\Sigma_{11}^0.
\end{aligned} \tag{8}$$

Again, we emphasize that $\Sigma_{\text{II}} > \Sigma_{\text{III}}$, which from Eq. ((8)) is seen to hold when $|\rho_s| > 0$. For pure axisymmetric stress states, i.e. when $\rho_s = 0$ the plane of localization is undetermined. However, here it is assumed to remain with its normal in the $X_1^0 - X_3^0$ plane.

The orientation of the principal stresses, defined by the angle α shown in Fig. 1, can be expressed in terms of T and L as

$$\tan \alpha = \sqrt{1 - L^2}/\left(\text{sign}(3T\sqrt{3 + L^2} - 4L) - L\right). \tag{9}$$

The ratio of the macroscopic stress components with reference to the inclined coordinate system $X_1X_2X_3$ will also remain fixed and constant during the loading history, as discussed above, and can

be expressed by tensorial transformation in terms of ρ_n, ρ_s and angle θ as

$$\begin{aligned}
\psi_1 &= \Sigma_{22}/\Sigma_{11} = \frac{\rho_n}{\cos^2\theta + \sin^2\theta\rho_n + \sin 2\theta\rho_s}, \\
\psi_2 &= \Sigma_{33}/\Sigma_{11} = \frac{\sin^2\theta + \cos^2\theta\rho_n - \sin 2\theta\rho_s}{\cos^2\theta + \sin^2\theta\rho_n + \sin 2\theta\rho_s}, \\
\psi_3 &= \Sigma_{13}/\Sigma_{11} = \frac{\cos\theta\sin\theta(\rho_n - 1) + \cos 2\theta\rho_s}{\cos^2\theta + \sin^2\theta\rho_n + \sin 2\theta\rho_s}.
\end{aligned} \tag{10}$$

Thus, for the case of a planar band with $\theta = 0$, Eq. (10) simplifies to Eq. (4) such that $\psi_1 = \psi_2 = \rho_n$ and $\psi_3 = \rho_s$.

Hence, for a band with a certain orientation θ and a stress state characterized by the stress triaxiality T and the Lode parameter L, the macroscopic stress ratios acting on the 3D unit cell boundaries are given by Eqs. (7) and (10), which is the strategy employed when loading the 3D unit cell shown in Fig. 1(e). This is accomplished by applying appropriate boundary conditions and prescribed displacement such that the stress ratios are kept constant, which is discussed next.

2.2. Deformation of the 3D unit cell

Relative to a fixed Cartesian frame, a material point is described by the coordinates X_i in the undeformed configuration and by the coordinates $x_i = X_i + u_i$ in the deformed configuration, where u_i denotes the displacements. Fig. 2(a) depicts how the 3D unit cell may deform under loading in a planar band indicating that the cell boundaries will not remain straight. Thus, fully periodic boundary conditions must be applied on faces with normal vectors in the X_2–X_3 plane, which will be given in detail in Section 2.3. Sufficiently remote from the band of imperfection, i.e. the layer of voids, homogeneous conditions are assumed to prevail ($\partial u_i/\partial X_j = \text{const.}$), where for instance $\partial u_1/\partial X_2 = \partial u_1/\partial X_3 = 0$. Such conditions are here assumed for the boundary surfaces $X_1 = \pm D_0$, which will remain straight and parallel throughout the loading.

Following the notation of Rice (1977), compatibility across the band requires in the present cell analysis that the displacement gradient with respect to X_1 on sides $X_3 = \pm D_0/2$ must take the form

$$\frac{\partial u_i}{\partial X_1} = \left(\frac{\partial u_i}{\partial X_1}\right)^o + q_i(X_1), \quad i = 1, 3, \tag{11}$$

where $(\;)^o$ denotes the uniform field quantities outside the band of localized deformation and q_i denotes the non-uniform part of the displacement gradient across the band, which is a function of X_1 only, see the illustration in Fig. 2(b). The volume average of the deformation gradient can be determined from the displacements on the cell boundary as
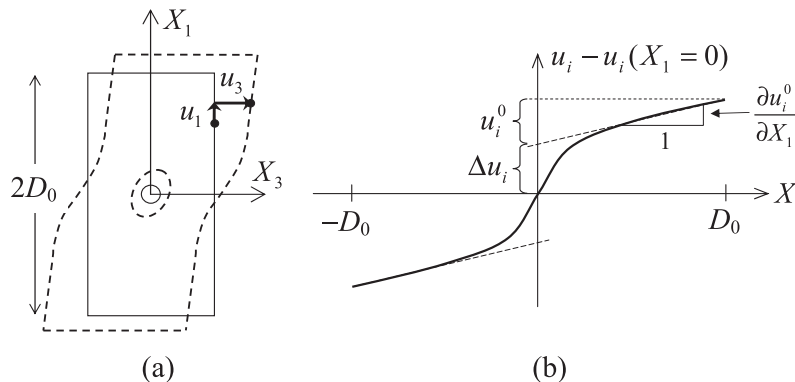

Fig. 2. (a) Depicting a general deformation mode of the unit cell in plane $X_2 = 0$ and (b) illustrating the uniform and non-uniform parts of the displacements, where $i = 1, 3$.

$$\overline{F}_{ik} = \frac{1}{V_0}\int_{V_0} F_{ik}\,dV_0 = \delta_{ik} + \frac{1}{V_0}\int_{S_0} u_i n_k^0\,dS_0, \tag{12}$$

where V_0 and S_0 are undeformed volume and outer surfaces of the cell, respectively, δ_{ik} denotes Kronecker delta and n_k^0 are components of the normal vector to S_0 in the undeformed configuration. In view of Fig. 2(b) and Eqs. (11) and (12), the volume average of the deformation gradient for the 3D unit cell can be expressed as

$$\overline{\mathbf{F}} = \mathbf{F}^0 + \overline{\mathbf{F}}^q = \begin{bmatrix} F_{11}^0 + \bar{q}_1 & 0 & 0 \\ 0 & F_{22}^0 & 0 \\ F_{31}^0 + \bar{q}_3 & 0 & F_{33}^0 \end{bmatrix} \quad \text{with } \bar{q}_i = \frac{\Delta u_i}{D_0}. \tag{13}$$

Here, $\mathbf{F}^0$ denotes the uniform deformation gradient outside the band of localized deformation, and hence localization of deformation into a narrow planar band can be defined as Needleman and Tvergaard (1992)

$$\eta = \left\| \dot{\overline{\mathbf{F}}} \right\| / \left\| \dot{\mathbf{F}}^0 \right\| \to \infty. \tag{14}$$

In Eq. (14) the norm $\| \, \|$ of a 2nd order tensor with components $(\,)_{ij}$ is evaluated as $\sqrt{(\,)_{ij}(\,)_{ij}}$ and for practical purposes localization is taken to occur when the ratio η is sufficiently large. In the present study a ratio of 10 was used.

As an effective scalar measure of strain was employed

$$E_e = \int \sqrt{\frac{2}{3} D'_{ij} D'_{ij}}\,dt, \quad D'_{ij} = D_{ij} - \frac{1}{3}\delta_{ij}D_{kk}, \tag{15}$$

where D_{ij} is the components of the volume average of the rate of deformation tensor, which can be calculated from the volume average of the deformation gradient as

$$D_{ij} = \frac{1}{2}\left(\dot{\overline{F}}_{ik}\overline{F}_{kj}^{-1} + \dot{\overline{F}}_{jk}\overline{F}_{ki}^{-1} \right). \tag{16}$$

The effective strain at localization will be a function of the inclination angle, therefore it is convenient to define the critical strain at localization for a certain inclination angle as $E_e^c(\theta)$. For a planar band with $\theta = 0$ the critical strain is denoted $E_e^c(\theta = 0)$ and for a band minimizing ductility the critical strain is denoted $E_e^c(\theta = \theta^c)$, where θ^c is the orientation giving minimum localization strain for a given stress state.

2.3. Numerical implementation

The 3D unit cell was numerically analyzed by use of the finite element program (ABAQUS, 2004). The material in the cell was assumed to be elastic–plastic with isotropic hardening, with the uniaxial behavior defined in Section 3 below. ABAQUS (2004) makes use of an updated Lagrangian formulation to account for large deformations and employs a finite strain J_2 flow theory, with an associated flow rule, based on a co-rotational stress rate to account for rotations of the principal axes of deformation.

Symmetry allows for modeling of the $X_2 \leqslant 0$ half of the unit cell. A typical mesh with $\chi_0 = 0.2$ is shown in Fig. 3. It consists of 5184 20-node tri-quadratic elements with reduced integration of which 432 are located on the half of the spherical void surface. Periodic boundary conditions are applied on the surfaces $X_3 = \pm D_0/2$. Four displacement measures δ_i ($i = 1, 2, 3, 4$) are introduced to describe the periodic and the homogeneous boundary conditions, respectively. The displacement boundary conditions can then be formulated as

$$\text{On } X_1 = \pm D_0: \quad \begin{aligned} u_1(D_0, X_2, X_3) &= -u_1(-D_0, X_2, X_3) = \delta_1, \\ u_2(D_0, X_2, X_3) &= u_2(-D_0, X_2, X_3), \\ u_3(D_0, X_2, X_3) &= u_3(-D_0, X_2, X_3) + 2\delta_4, \end{aligned} \tag{17}$$
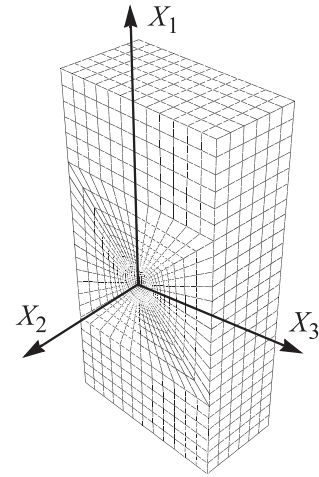

Fig. 3. Finite element mesh of one half of the unit cell.

$$\text{On } X_3 = \pm D_0/2: \quad \begin{aligned} u_1\left(X_1, X_2, \tfrac{D_0}{2}\right) &= u_1\left(X_1, X_2, \tfrac{-D_0}{2}\right), \\ u_2\left(X_1, X_2, \tfrac{D_0}{2}\right) &= u_2\left(X_1, X_2, \tfrac{-D_0}{2}\right), \\ u_3\left(X_1, X_2, \tfrac{D_0}{2}\right) &= u_3\left(X_1, X_2, \tfrac{-D_0}{2}\right) + \delta_3, \end{aligned} \tag{18}$$

$$\begin{aligned} \text{On } X_2 = 0: \qquad & u_2(X_1, 0, X_3) = 0, \\ \text{On } X_2 = -D_0/2: \quad & u_2\left(X_1, \tfrac{-D_0}{2}, X_3\right) = \delta_2/2. \end{aligned} \tag{19}$$

Utilizing Eqs. (17)–(19) in Eq. (12), the volume average of the deformation gradient and the velocity gradient, respectively, can be expressed as

$$\overline{\mathbf{F}} = \begin{bmatrix} \frac{D_1}{D_0} & 0 & 0 \\ 0 & \frac{D_2}{D_0} & 0 \\ \frac{\delta_4}{D_0} & 0 & \frac{D_3}{D_0} \end{bmatrix}, \quad \overline{\mathbf{L}} = \dot{\overline{\mathbf{F}}}\,\overline{\mathbf{F}}^{-1} = \begin{bmatrix} \frac{\dot{\delta}_1}{D_1} & 0 & 0 \\ 0 & \frac{\dot{\delta}_2}{D_2} & 0 \\ \frac{\dot{\delta}_4}{D_1} - \frac{\dot{\delta}_3}{D_3}\frac{\delta_4}{D_1} & 0 & \frac{\dot{\delta}_3}{D_3} \end{bmatrix}, \tag{20}$$

where $D_1 = D_0 + \delta_1$, $D_2 = D_0 + \delta_2$ and $D_3 = D_0 + \delta_3$. The symmetric part of $\overline{\mathbf{L}}$ defines the volume average of the rate of deformation tensor $\mathbf{D}$, (16).

Here, the rates of δ_i are determined from the condition of loading under fixed stress ratios according to Section 2.1. The numerical procedure for implementing the special type of boundary conditions will not be addressed here. The method is outlined in Barsoum and Faleskog (2007b).

3. Material

Two materials are considered, one corresponding to a medium strength steel with moderate hardening and one corresponding to a high strength steel with low hardening. The true stress–strain behavior is given by Eq. (21) for both the materials, where σ_0 represents the initial yield stress, N strain hardening exponent and $\varepsilon_0 = \sigma_0/E$, with E being Young's modulus. These material parameters are listed in Table 1.

$$\sigma = \begin{cases} E\varepsilon, & \varepsilon \leqslant \varepsilon_0, \\ \sigma_0\left(\frac{\varepsilon}{\varepsilon_0}\right)^N, & \varepsilon > \varepsilon_0. \end{cases} \tag{21}$$

It is assumed that voids will nucleate from inclusions embedded in the matrix material. It should be noted, however, that not all

Table 1
Material parameters for the two materials considered (Eq. (21)).

	N	ε_0
Material 1	0.05	0.0050
Material 2	0.10	0.0025

inclusions will contribute to nucleation of voids. For such steels considered here, typically the volume fraction of inclusions is in the range 0.03–0.7% (Barsoum and Faleskog, 2007b; Garrison and Moody, 1987), which corresponds to an initial void size to void spacing ratio χ_0 in the range 0.1–0.3. Thus an initial void size to void spacing ratio $\chi_0 = 0.2$ is used in the micromechanical analysis, which is a representative fraction of inclusions participating in nucleating voids in these materials.

4. Results: localization into the plane of axisymmetry ($\theta = 0$)

Here the localization behavior and results pertaining to a planar band with $\theta = 0$ will be presented. Such an over constraint case, where a relatively thin layer of material is confined between two blocks of materials preventing a change in the direction of localization is found, e.g. in the double notched tube experiments reported by Barsoum and Faleskog (2007a). There the fractographs reveal a rather flat fracture surfaces indicating that localization occurs in the plane of axisymmetry between the notch roots, at least on a macroscopic level in the lower stress triaxiality regime. Another example when an initial planar band is prevented from changing direction of localization is in voided polymer blends, where the polymer acts as an adhesive layer between two material blocks of higher stiffness (Pijnenburg and Van der Giessen, 2001; Ferracin et al., 2003).

In order to gain a more general understanding of the influence of the Lode parameter on localization, a systematic investigation covering the entire span in the Lode parameter, $-1 \leqslant L < 1$, is here performed for various levels of stress triaxiality. In Fig. 4 the localization locus in terms of the effective strain at the onset of localization $E_e^c(\theta = 0)$, given by the criterion in Eq. (14) is plotted vs. L for Material 1 and Material 2 in Fig. 4(a) and (b), respectively. The results correspond to $\chi_0 = 0.2$, $\theta = 0$ and $T = 0.75, 1, 1.5$ and 2. As shown $E_e^c(\theta = 0)$ decreases with increasing T, as would be expected. For the Lode parameter in the interval $-1 \leqslant L \leqslant 0$, ranging from axisymmetric tension to a pure shear stress state with superimposed hydrostatic tension, $E_e^c(\theta = 0)$ decreases with increasing L and reaches a minimum close to $L = 0$. However, beyond this point $E_e^c(\theta = 0)$ increases drastically for increasing positive L values. Here the localized deformation shifts gradually from a shear to a biaxial deformation mode and for $L \to 1$ the deformation will not localize across the planar band of voids. The stress strain response of the unit cell is virtually unaffected by the presence of voids at high T values when $L \to 1$.

4.1. Influence of the Lode parameter on void growth and coalescence

To exemplify the influence of L on the stress–strain response, void growth and localization behavior results pertaining to Material 1 are

shown in Fig. 5 for an intermediate stress triaxiality level $T = 1$ and an initial void size to void spacing ratio $\chi_0 = 0.2$. Here, attention is again restricted to a planar band with $\theta = 0$. Seven different L values are considered, $L = -1, -0.75, -0.5, -0.25, 0, 0.25, 0.5$.

As can be seen from Fig. 5(a), the macroscopic effective stress–strain behavior is strongly effected by L. During the deformation a competition between hardening of the matrix material and softening due to void growth takes place. As deformation progresses a maximum effective stress is reached prior to the onset of localization. The effective stress decreases as the hardening of the matrix material is insufficient to compensate for the reduction in intervoid ligament caused by void growth. For $-1 \leqslant L \leqslant 0$ the strain to localization decreases with increasing L as shown in Fig. 5(b) where the ratio η in Eq. (14) is plotted vs. E_e for the different L values considered. For $L = -1$ localization occurs at $E_e = 0.43$, whereas for $L = 0$ localization occurs at $E_e = 0.14$ at $\eta = 10$. Furthermore, the softening rate in the post-localization regime increases with decreasing L as can be seen in Fig. 5(a). This is closely connected to the increase in void growth rate, which can be appreciated from Fig. 5(c) where the quotient between current to initial void volume V_v/V_{v0} vs. E_e is depicted. The void growth rate is the slope of these curves. For the case $L = -1$ the void growth rate is initially low but increases drastically at the onset of localization giving rise to significant softening. For increasing L, $L = -0.75, -0.5$ and -0.25, the initial void growth rate increases leading to softening at an earlier stage during the deformation history. However, the drastic increase in void growth rate associated with the onset of localization lessens with increasing L. For the case $L = 0$ the onset of localization occurs at a rather early stage of deformation followed by an intermediate rate of void growth and hence a less significant rate of softening.

Fig. 5(d) and (e) shows the deformation measures $\bar{q}_1$ and $\bar{q}_3$ vs. E_e corresponding to the non-uniform normal and shear deformation, respectively. The mode of deformation, whether normal, shear or a combination of both can be apprehended from these two figures. For the case of $L = -1$, $q_1 > 0$ and $q_3 = 0$ indicating pure axisymmetric deformation, as would be expected. Increase in L, i.e. $L \to 0$, gives increase in shear deformation. At $L = 0.5$ the normal and shear deformation measures attain values $q_1 < 0$ and $q_3 > 0$, which indicates a compressive shear deformation mode. As can be seen from Fig. 5(b) the deformation does not localize across the band, which is a consequence of a positive value of L. Here the rapid increase in void growth is due to that deformation takes place within the planar band in the X_2 and X_3 directions of the unit cell. Hence q_1 and q_3 gradually looses the purpose of being valid parameters for localized deformation for increasing positive L. Not shown here, for lower stress triaxiality and positive L, i.e. $T = 0.5$ and $L > 0$, the void growth is very limited and no localization point can be identified. As a consequence of the compressive deformation mode and low level of hydrostatic stress self-contact of the
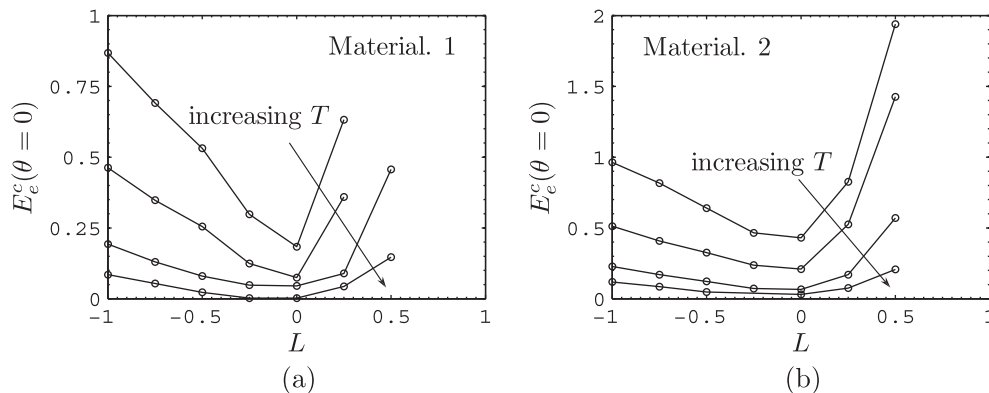

Fig. 4. Localization loci for (a) Material 1 and (b) Material 2 with $\chi_0 = 0.2$, $\theta = 0$ and $T = 0.75, 1, 1.5$ and 2.
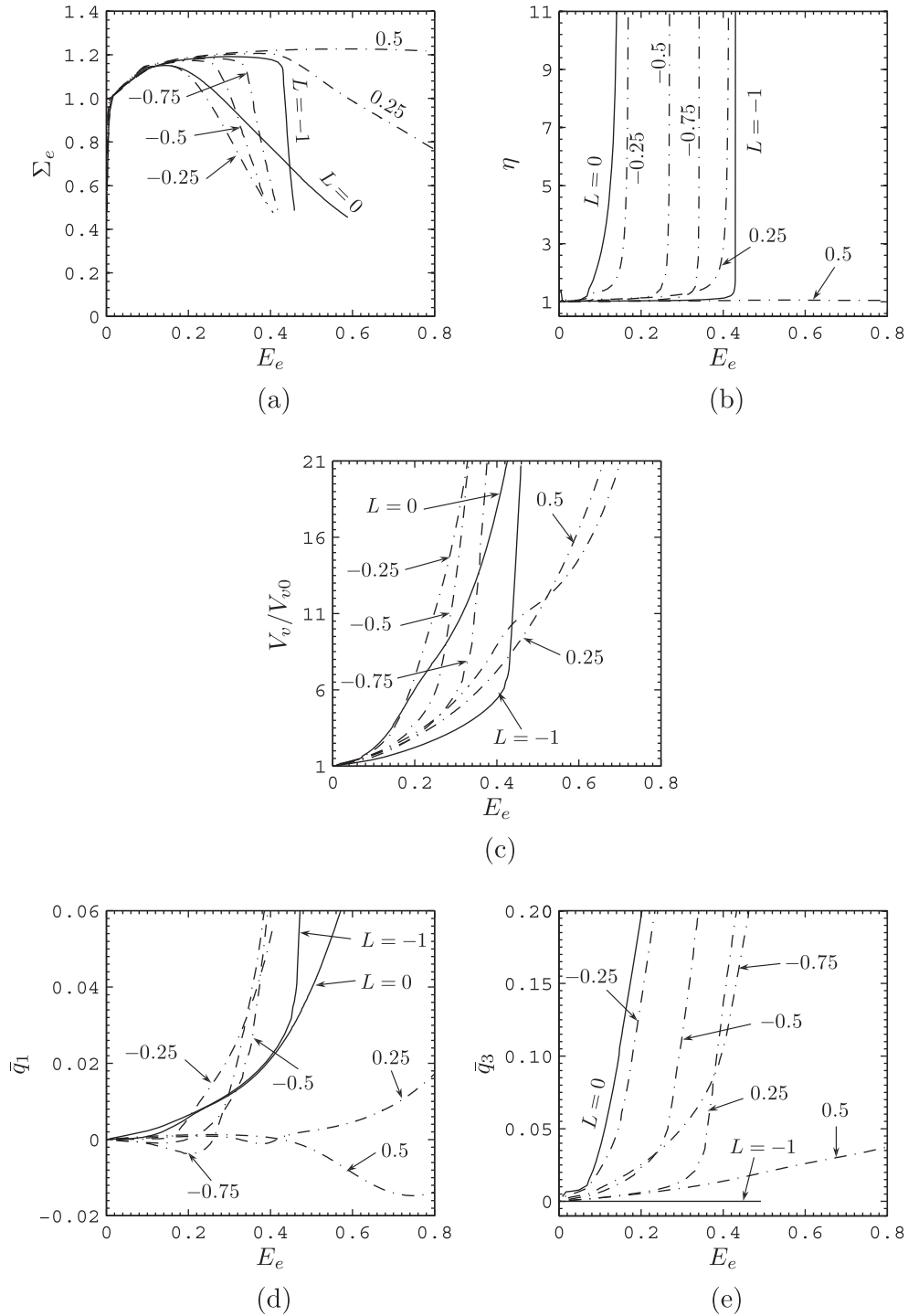
Fig. 5. Influence of the Lode parameter on the model behavior for Material 1 with $\chi_0 = 0.2$, $T = 1.0$ and $\theta = 0$. Showing (a) macroscopic effective stress, (b) the ratio η in Eq. (14), (c) void growth, (d) $\bar{q}_1$ and (e) $\bar{q}_3$ vs. macroscopic effective strain.

void surface is encountered. In such situation the presence of a void-nucleating particle or inclusion is crucial, which is reported by Tvergaard (1989), Tvergaard (2009b), Tvergaard (2009a), Siruguet and Leblond (2004a), Siruguet and Leblond (2004b) and McVeigh et al. (2007) among others.

4.2. Equivalent plastic strain field in the void cell

In Figs. 6 and 7 the contours of the equivalent plastic strain are shown at different stages throughout the deformation illustrating

the development of the localization process. Fig. 6 corresponds to $T = 1$ and $L = -1$ showing the distribution of the equivalent plastic strain at the pre-localization stage or void growth stage in (a), at the onset of localization in (b) and at the post-localization stage or void coalescence stage in (c). During the void growth stage the plastic deformation has not yet localized in a band and is homogeneously distributed around the void. Once the localization takes place, the plastic strain is confined to a band with a thickness approximately of the size of the void spacing. At the post-localization stage in Fig. 6(c) the void has grown considerably with plastic flow
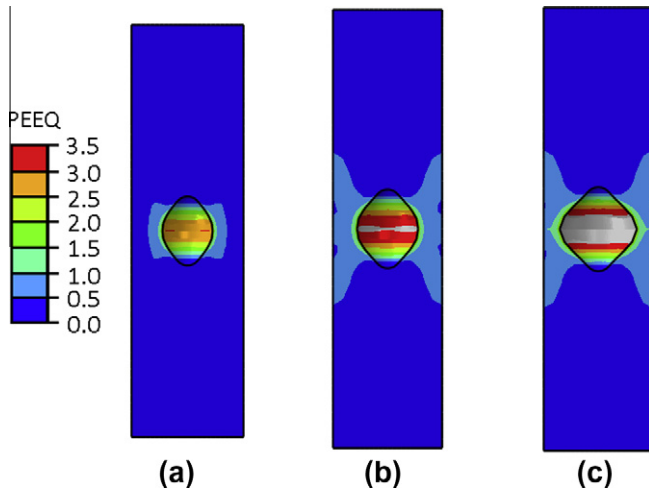
Fig. 6. The distribution of the equivalent plastic strain around the void for $T = 1$ and $L = -1$ at different loading stages: (a) pre-localization and void growth stage, (b) at localization ($\eta = 10$) and (c) post-localization.

localizing in the ligament between the voids leading to final coalescence by internal necking of the intervoid ligaments.

However, Fig. 7 corresponding to $T = 1$ and $L = 0$ shows a distinctly different evolution of the plastic strain field during localization. Fig. 7(a) shows the plastic strain at the pre-localization stage indicating no localization of plastic flow in the intervoid ligament. With progress of deformation plastic flow localizes in a rather narrow band as shown in Fig. 7(b) where the void has undergone limited growth. With further progress of the deformation shown in Fig. 7(c) the void undergoes considerable shearing and plastic flow localizes and increases markedly in the intervoid ligament. As indicated by Fig. 7(c) and reported in Barsoum and Faleskog (2007b) the final rupture takes place by shearing of the intervoid ligament, assumably by secondary void nucleation within the intervoid ligament. However, the process of void nucleation is not considered in the present micromechanical model.

5. Results: Localization into a plane minimizing ductility ($\theta = \theta^c$)

Here the influence of the Lode parameter and band orientation on localization is explored using the 3D computational unit cell. The objective is to find the band orientation that gives rise to the minimum localization strain over all possible band orientations within the framework of the simplified approach discussed in Section 2. The minimum of the localization strain gives the critical strain and direction at which the inception of localization is first possible for a certain stress state characterized by T and L. Hence, the dependence of the critical localization direction and critical
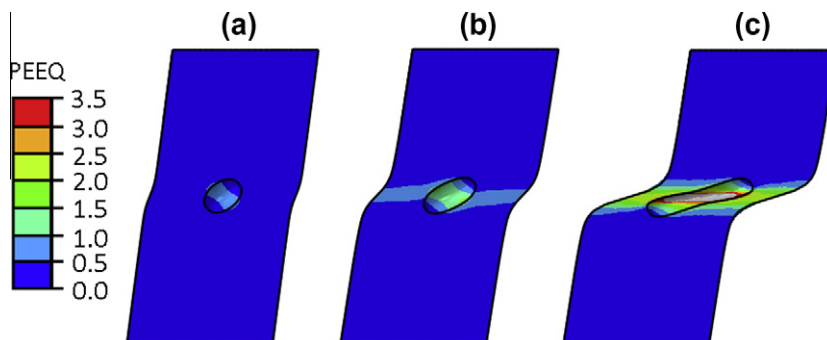
strain on T and L is sought for. Fig. 8 depicts the localization strain $E_e^c(\theta)$ as function of the band orientation θ for various L values and a constant stress triaxiality level $T = 1$. The solid lines and dashed lines correspond to material 1 and 2, respectively, and the dots correspond to the numerical analyses. The localization strain depends strongly on the band orientation for all L values. For the axisymmetric stress states $L = \pm 1$, the relation $E_e^c(\theta)$ vs. θ is not unambiguous since all bands with the same inclination with respect to the axis of symmetry (X_1) will be equally critical. Not shown here, but the magnitude and the shape of the curves are also dependent on the level of triaxiality. Typically, lower T-values give rise to higher localization strains with curves of more narrow shape and by contrast higher T-values give rise to lower localization strains with curves of more open shape.

The minima of the curves determine the most critical inclination angle and the lowest possible localization strain denoted θ^c and $E_e^c(\theta = \theta^c)$, respectively. These were obtained by determining the minimum of the spline interpolation curves fitted onto the data points from the numerical analyses such as in Fig. 8. Four different stress triaxiality levels $T = 0.75, 1, 1.5$ and nine different L values $L = -1, -0.75, -0.5, -0.25, 0, 0.25, 0.5, 0.75, 1$ for both materials were considered. Fig. 9(a) and (b) shows the critical inclination angle θ^c and φ^c, respectively, vs. L. The dots correspond to minimum values of curves such as in Fig. 8 for all T values considered and both materials with $\chi_0 = 0.2$. As revealed from Fig. 9(a) the critical inclination angle of the band θ^c depends strongly and only on L and takes on θ^c values of about 37°, 0° and −53° for $L = -1, 0$ and +1, respectively.

Interestingly, the shape of the curve φ^c vs. L in Fig. 9(b) is close to symmetric about $L = 0$, with $\varphi^c = 45°$ for $L = 0$ and $\varphi^c \approx 37°$ for $L = \pm 1$. The solid line is a third order polynomial fit to the numerical data such that $\varphi^c = 45°$ for $L = 0$ given as Eq. (22). The modest scatter in the data points does not show a systematic trend with respect to T and is mainly due to the numerical evaluation procedure of finding the minimum of the curves based on discrete data as shown in Fig. 8.

Eq. (22) shown in Fig. 9(b) differs at most with 1.6° from the data points. For $L = \pm 1$, φ^c attains the value 37°, as also reported by Rudnicki and Rice (1975). For $L = 0$, φ^c attains the value 45°, which is also observed by Nahshon and Hutchinson (2008). Tvergaard (1989) also finds this value for the case of uniaxial plane strain tension. Thus, it appears that φ^c is rather independent of the level of stress triaxiality and the mechanical properties of the undamaged material between the voids. This implies that the direction at which the inception of localization is first possible is only affected by the deviatoric stress state parameter L and given by

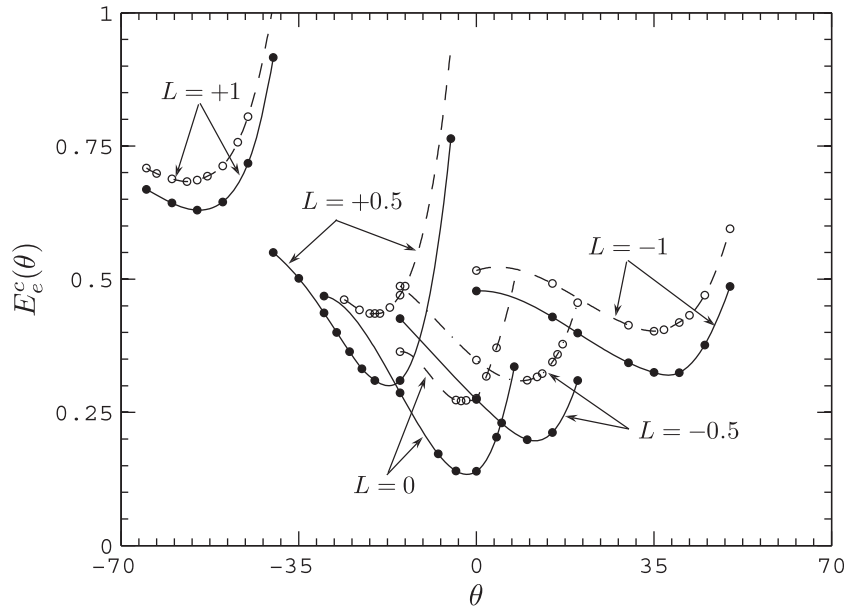$$\varphi^c = 45° \left(1 - 0.29|L| + 0.32L^2 - 0.20|L|^3\right). \quad (22)$$

Fig. 7. The distribution of the equivalent plastic strain around the void for $T = 1$ and $L = 0$ at different loading stages: (a) pre-localization and void growth stage, (b) at localization ($\eta = 10$) and (c) post-localization.

Fig. 8. Localization strain vs. the band inclination angle θ for different L values with $T = 1$ and $\chi_0 = 0.2$. The solid lines correspond to Material 1, the dot-dashed lines to Material 2 and dots correspond to numerical analyses.
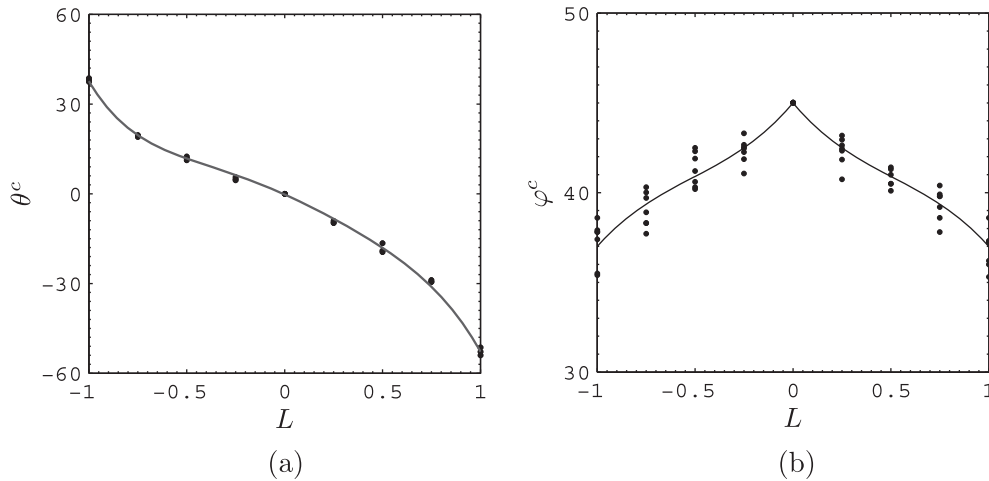

Fig. 9. Critical band orientation (a) θ^c vs. L and (b) φ^c vs. L. Results are for all T values considered and both materials. The solid line corresponds to Eq. (22).

5.1. Influence of the Lode parameter on critical localization strain

L and T have a significant effect on the critical localization strain, which is evident from the localization loci shown in Fig. 10(a) and (b) for material 1 and 2, respectively, where the critical localization strain $E_e^c(\theta = \theta^c)$ vs. L for $T = 0.75$, 1, 1.5 and 2 is shown. As could be expected the stress triaxiality has a strong influence on the magnitude of the critical localization strain such that high T values give rise to low localization strain and vice versa, with a similar trend as was found in Fig. 4. However, regardless the level of stress triaxiality, Fig. 10 shows that $E_e^c(\theta = \theta^c)$ has a minimum at about $L = 0$ and a maximum at $L = +1$. Fig. 10 indicates that the most critical state of stress from a localization point of view experienced in a ductile solid is for a pure or near a pure shear stress state $L = 0$, where material failure will occur at an angle close to $\varphi^c = 45°$ with respect to the direction of the smallest principal stress according to Fig. 9(b).

It is interesting to note that for a constant stress state a planar band ($\theta = 0$), Fig. 4, shows a much higher localization strain in comparison with a band localizing in the direction $\varphi = \varphi^c$ ($\theta = \theta^c$) min-

imizing ductility in Fig. 9. However, for stress states with L close to zero and a high level of T, the critical localization strains are unrealistically low if they would be regarded as the instant of ductile failure, as will be evident in Section 5.2.

5.2. Influence of the Lode parameter on mechanical behavior

Here the mechanical behavior of the model is explored at the critical localization direction $\varphi = \varphi^c$ and is depicted in Fig. 11 for $T = 1$ and Fig. 12 for $T = 2$. The figures pertain to results for Material 1 with $\chi_0 = 0.2$, $L = 0$ and $L = \pm 1$. The macroscopic effective stress strain response and the void growth are strongly affected by L, as can be seen in Fig. 11(a) and (b) respectively, where the open circles represent the onset of localization. The sudden increase in softening is associated with the onset of localization. The significant increase in softening rate in the post-localization regime is closely connected to the void growth rate as can be appreciated from the slopes of the curves in Fig. 11(b), showing the ratio between current to initial void volume V_v/V_0 vs. E_e. For $L = -1$ localization occurs at about $E_e = 0.32$ followed by a significant softening
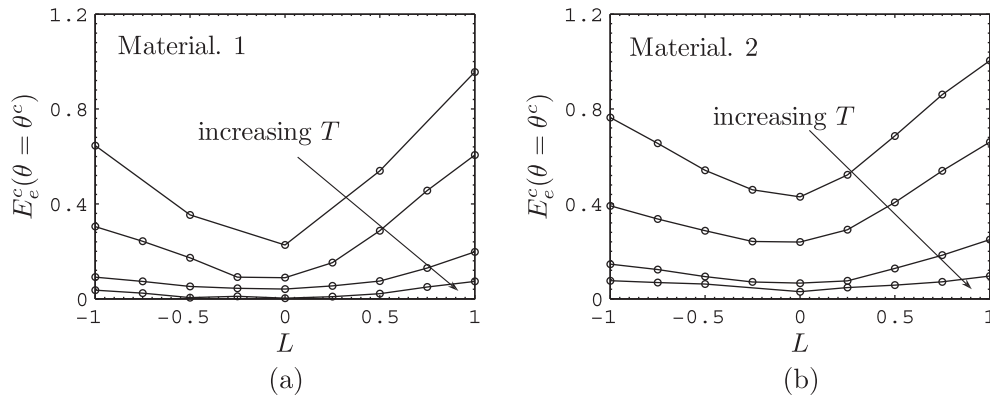
Fig. 10. Localization loci for (a) Material 1 and (b) Material 2 with $\chi_0 = 0.2$, at $\varphi = \varphi^c$ and $T = 0.75$, 1, 1.5 and 2.

due the drastic increase in void growth rate in the post-localization stage. For $L = 0$, where localization occurs earlier at about $E_e = 0.14$, the softening is not as marked and the void growth rate increases gradually with no drastic changes. However, for $L = +1$ the onset of localization is delayed and occurs at about $E_e = 0.63$. Despite the fact that the void has undergone extensive growth at $V_v/V_0 = 33$ at this point. Beyond this point the extensive void growth is manifested in a drastic increase in the softening rate.

Fig. 11(b) shows the deformation jumps across the band, $\bar{q}_1$ (dashed line) and $\bar{q}_3$ (solid line) vs. E_e. Prior to localization the deformation is homogeneous and thus $\bar{q}_i$ are negligible. However,

when deformation begins to localize $\bar{q}_i$ increase and the mutual increase between $\bar{q}_1$ and $\bar{q}_3$ reveals the dominating deformation mode, whether normal or shear localization. When $\bar{q}_3 \gg \bar{q}_1$ shear localization dominates whereas when $\bar{q}_1 \gg \bar{q}_3$ normal localization dominates. Fig. 11(c) shows that $\bar{q}_3 \gg \bar{q}_1$ for all L, which indicates that the dominating deformation mechanism is shear localization.

For the higher stress triaxiality level $T = 2$ in Fig. 12, the behavior is slightly different. Onset of localization coincides with the onset of plastic loading for $L = 0$, as shown in Fig. 12(a). In the post-localization regime the void growth is extensive and less influenced by L as can be seen from Fig. 12(b). As indicative from
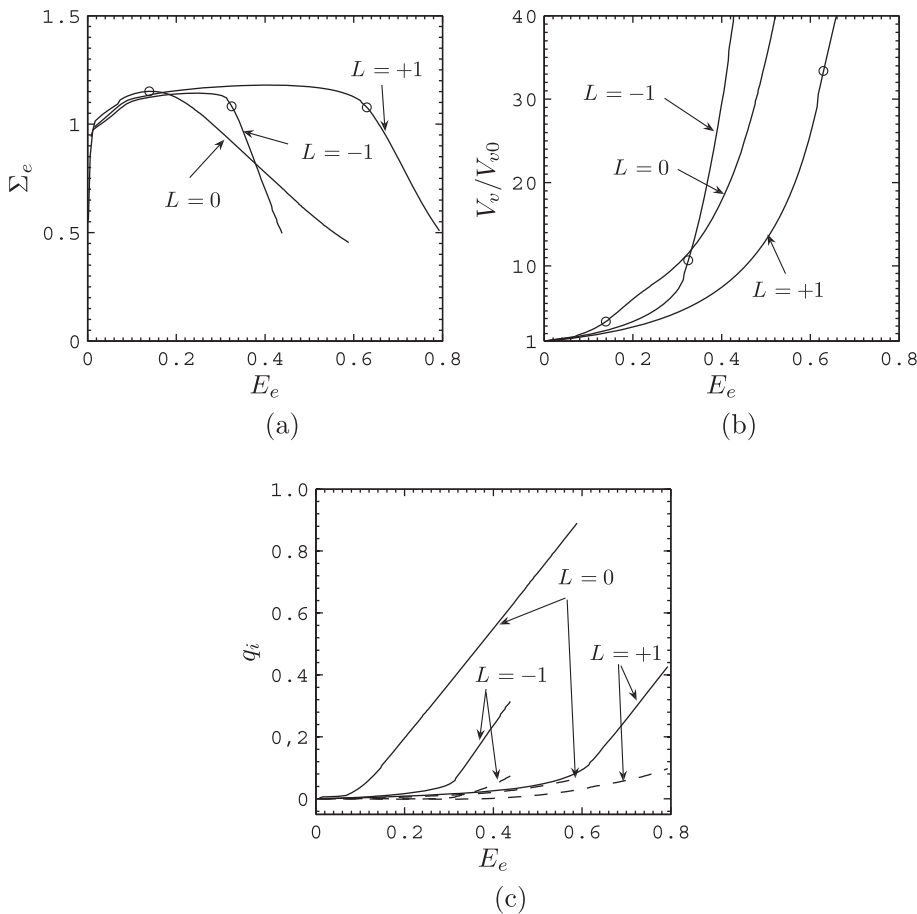

Fig. 11. Influence of L on the model behavior for Material 1 at the critical localization direction $\varphi = \varphi^c$ with $\chi_0 = 0.2$ and a constant triaxiality $T = 1.0$. Showing (a) macroscopic effective stress, (b) void growth and (c) the localized deformation parameters $\bar{q}_i$ vs. macroscopic effective strain. In (c) the solid lines correspond to $\bar{q}_3$ and the dashed lines to $\bar{q}_1$.
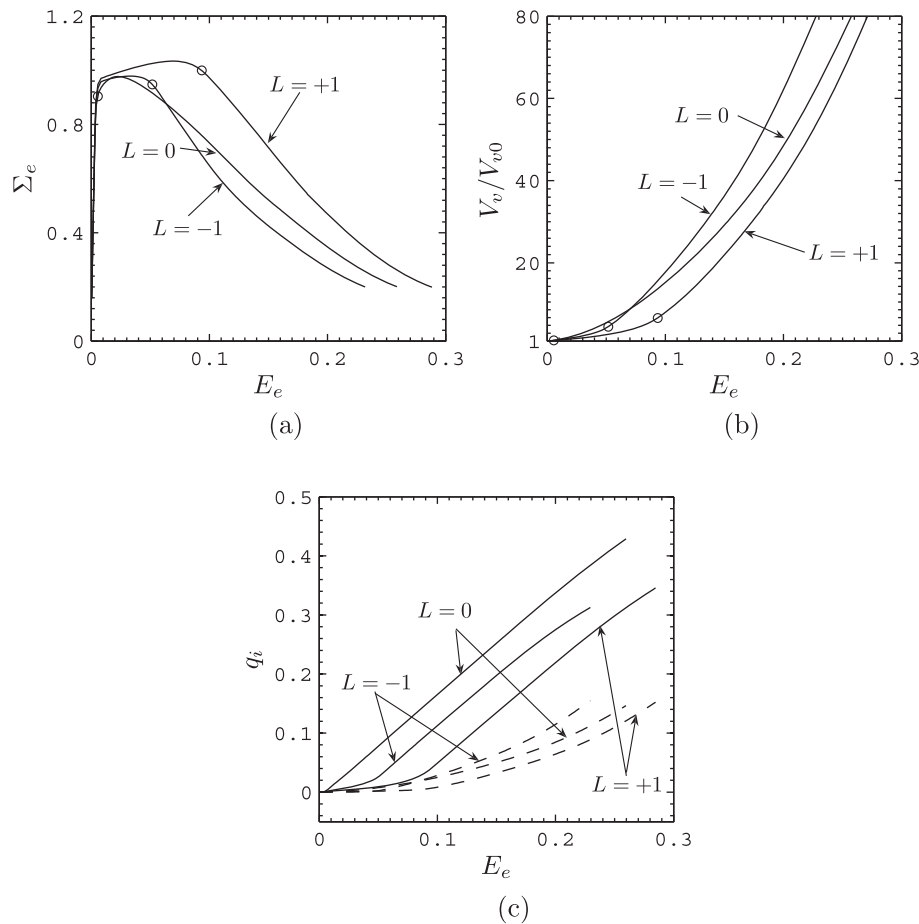
Fig. 12. Influence of L on the model behavior for Material 1 at the critical localization direction $\varphi = \varphi^c$ with $\chi_0 = 0.2$ and a constant triaxiality $T = 2.0$. Showing (a) macroscopic effective stress, (b) void growth and (c) the localized deformation parameters $\bar{q}_i$ vs. macroscopic effective strain. In (c) the solid lines correspond to $\bar{q}_3$ and the dashed lines to $\bar{q}_1$.

Fig. 12(c), the deformation modes are a combination of normal and shear localization.

5.3. Influence of the Lode parameter on void shape

The effect of void shape on the mechanical behavior has been studied by a number of authors in the past. One of the early attempts is made by Gologanu et al. (1996) where they extend the Gurson model, which is based on solutions for voids under axisymmetric conditions, to account for ellipsoidal void growth. Pardoen and Hutchinson (2000) make use of the extended Gurson model in combination with an axisymmetric coalescence model first proposed by Thomason (1985) and find that void shape has a strong effect on localization and coalescence. Zhang et al. (2001) among others use a three dimensional cell with an initially spherical void and also find that L has a great influence on the evolution of the void shape. Void growth under dominated shear deformation, however, has not been thoroughly addressed in the past. Here the effect of L on the void shape evolution is explored with the current computational cell model allowing for shear deformation.

In Figs. 13 and 14 the effect of L and T on the void shape and void shape evolution is shown. Two stress triaxiality levels are considered, where the results in Fig. 13(a)–(c) correspond to $L = -1$, 0 and +1, respectively with $T = 1$ whereas results in Fig. 14(a)–(c) correspond to $L = -1$, 0 and +1 with $T = 2$. In the set of sub-figures in the left column of Figs. 13 and 14 the void shape contours with the deformed cell boundaries are shown at the symmetry plane $X_2 = 0$. In the middle column the void contours at the outermost

contour of the projected void shape on the $X_1 = 0$ plane are displayed. The void contours are plotted at three different stages of loading, where the dashed lines correspond to the initial spherical void contours, dot-dashed lines to void contours at onset of localization and solid lines to void contours at effective stress Σ_e equal to 75% of its overall maximum in the post-localization regime. In the set of sub-figures in the very right column the void shape evolution r_a/r_c (solid lines) and r_b/r_c (dot-dashed lines) vs. E_e is depicted. Here r_a and r_c are the minimum and maximum distances between the origin and a point on the void contour at the symmetry plane ($X_2 = 0$), respectively, and r_b is the distance between the origin and the point on the void contour intersecting the X_2 axis. The open markers correspond to onset of localization and the solid markers to the instant when $\Sigma_e = 0.75 \max(\Sigma_e)$ in the post-localization regime.

For $T = 1$ the void contour in Fig. 13 shows that the initially spherical void undergoes excessive growth and shape change as the deformation progress, where the distorted void shape arises from the intense shear deformation (cf. Fig. 11(c)). For all L values Fig. 13(a)–(c) the void gradually shifts from spheroidal to ellipsoidal void growth up to the onset of localization as can be apprehended from the lines r_a/r_c and r_b/r_c vs. E_e. Beyond this point the void becomes highly distorted and rotated and approaches a penny-like shape. Especially for $L = 0$ in (b) and $L = +1$ in (c), where $r_a \leqslant R_0$, indicate that the presence of a void nucleating particle would affect the void growth behavior and void shape evolution. An interesting feature captured by Fig. 13 (left column) is the reduction of the intervoid ligament. The void will impinge with
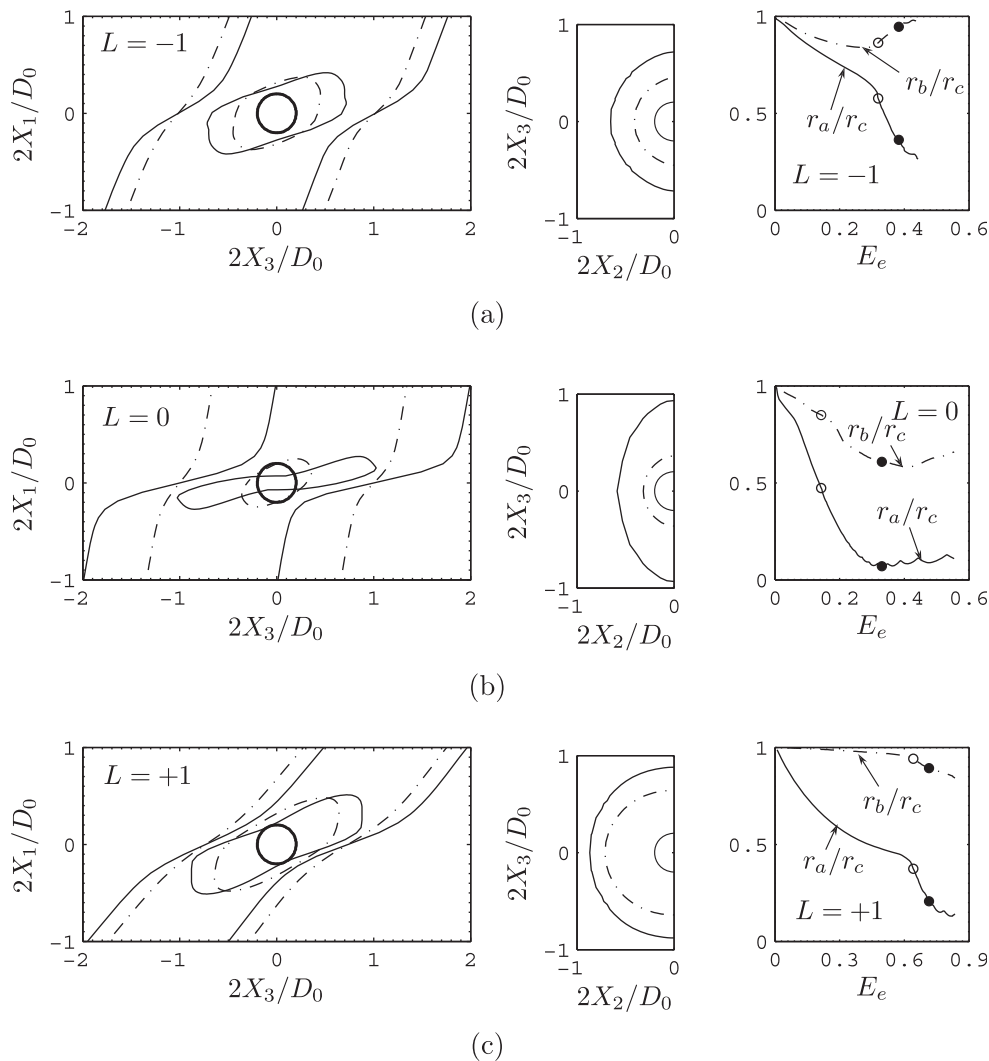
Fig. 13. Void shape evolution corresponding to Material 1, $\chi_0 = 0.2$ and $T = 1$ at $\varphi = \varphi^c$ with: (a) $L = 0$, (b) $L = -1$ and (c) $L = +1$. In the left column of sub-figures the void contours at the symmetry plane $X_2 = 0$ are shown and in the middle column the void contours of the projected void shape on the $X_1 = 0$ are shown. Dot-dashed lines are at the onset of localization, solid line at $\Sigma_e = 0.75\max(\Sigma_e)$ and dashed lines depict the initial void. In the left column the void shape evolution r_a/r_c and r_a/r_c vs. E_e are shown.

its neighboring voids across the smallest intervoid ligament section at the final stage of rupture. This have been shown in a recent study by Weck et al. (2006), where the voids coalesce by internal shearing. Weck et al. (2006) investigate experimentally the void shape evolution in a metallic plate with laser-drilled array of micro-holes aligned 45° with respect to the tensile loading axis. The experimentally observed shape of the deformed micro-holes at the coalescence event resembles the deformed void shape contour shown in Fig. 13(b) with solid lines at the left column.

For a higher level of stress triaxiality, i.e. $T = 2$ in Fig. 14, the influence of L on the void shape evolution is not as marked as for $T = 1$ in Fig. 13. As seen from the void evolution curves at the right column of Fig. 14, $r_b/r_c \geqslant 1$ throughout the entire deformation history, which indicates that the void grows faster in the X_3 direction of the unit cell than in the symmetry plane. As the deformation progresses the ratio r_b/r_c increases, reaches a maximum value of about 1.2 and decreases to about 1, whereas r_a/r_c decreases monotonically and reaches a stationary value between 0.4 and 0.5. This corresponds to a nearly spherical void growth. Hence the void shape evolution is less sensitive to L for increasing T as revealed by comparison of Figs. 13 and 14. Similarly, comparison of Fig. 11(b) and Fig. 12(c) reveals that the influence of L on the void growth rate is also reduced for increasing T.

Moreover, for the case of $T = 1$ and $L = 0$ in Fig. 13(c) it is seen from the void contour that the void has undergone limited void growth at the onset of localization (dot-dashed lines). This is even more apparent for $T = 2$ and $L = 0$ in Fig. 14(c), where the onset of localization coincides with onset of plastic loading and the void growth is negligible. Therefore onset of localization cannot be viewed as a void coalescence criterion for $L = 0$. This primarily due to the fact that the micromechanical model used in the current study disregards the existence of a volume fraction of voids outside the band of localization. Existence of voids outside the band would effect the localization behavior significantly as reported by Nahshon and Hutchinson (2008). However, it is clear by now that an additional void coalescence criterion for shear dominated stress state is needed.

6. Conclusions

In this study the influence of the Lode parameter on ductile material failure, which is assumed to occur when deformation localizes into a thin void-containing band, is investigated. This was accomplished by utilizing a micromechanical model consisting of a three dimensional unit cell containing a single spherical
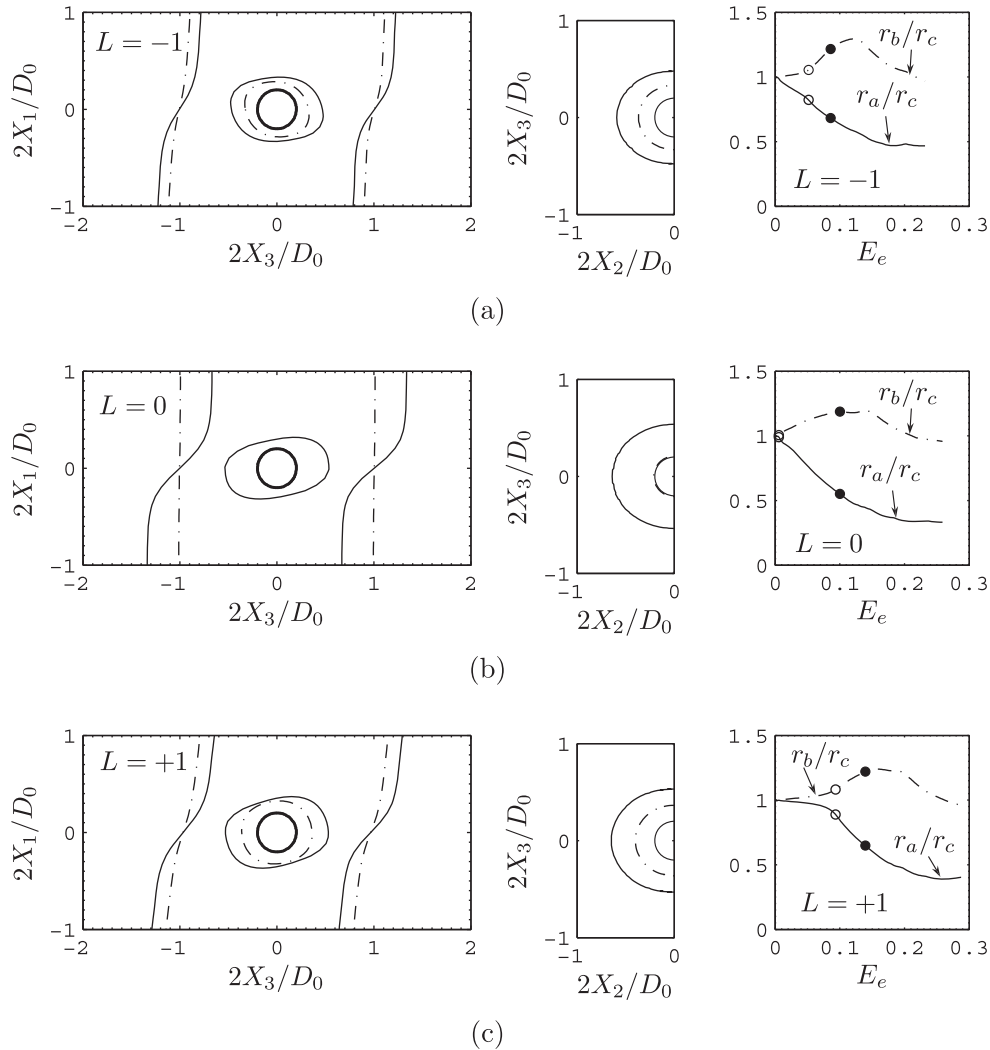
Fig. 14. Void shape evolution corresponding to Material 1, $\chi_0 = 0.2$ and $T = 2$ at $\varphi = \varphi^c$ with: (a) $L = 0$, (b) $L = -1$ and (c) $L = +1$. In the left column of sub-figures the void contours at the symmetry plane $X_2 = 0$ are shown and in the middle column the void contours of the projected void shape on the $X_1 = 0$ are shown. Dot-dashed lines are at the onset of localization, solid line at $\Sigma_e = 0.75 \max(\Sigma_e)$ and dashed lines depict the initial void. In the left column the void shape evolution r_a/r_c and r_a/r_c vs. E_e are shown.

void allowing for fully periodic boundary conditions. The unit cell is loaded under proportional loading conditions allowing for arbitrary stresses in terms of stress triaxiality, the Lode parameter and the band inclination angle. The present study is concluded in the following:

- The effect of L on the void shape evolution and void growth rate increases with decreasing level of stress triaxiality. At moderate triaxiality levels L has a strong influence on the mechanical behavior of the voided band.
- For dominating shear stress states, L close to 0, and high levels of T the localization criterion in Eq. (14) cannot be viewed upon as a void coalescence criterion predicting material failure. Here a micromechanical based coalescence criterion operative at dominating shear stress states is needed.
- In the current study void nucleation has not been considered. However, it has been shown in recent experimental studies (Barsoum and Faleskog, 2007a; Giovanola et al., 2006) that nucleation can be crucial in the last stage of the ductile material failure process, particularly at low stress triaxiality and dominating shear stress state. Hence, it appears to be necessary to account for void nucleation with a L and T dependent void nucleation model.

References

ABAQUS, 2004. Standard-User's Manual, Version 6.4. Hibbit. Karlsson and Sorensen, Inc., Providence, RI.
Barsoum, I., Faleskog, J., 2007a. Rupture mechanisms in combined tension and shear—experiments. International Journal of Solids and Structures 44 (6), 1768–1786.
Barsoum, I., Faleskog, J., 2007b. Rupture mechanisms in combined tension and shear—micromechanics. International Journal of Solids and Structures 44 (17), 5481–5498.
Cox, T.B., Low, J.R.J., 1974. An investigation of the plastic fracture of AISI 4340 and 18 nickel-200 grade maraging steels. Metallurgical Transactions 5 (6), 1457–1470.
Faleskog, J., Shih, C.F., 1997. Micromechanics of coalescence—I. Synergistic effects of elasticity, plastic yielding and multi-size-scale voids. Journal of Mechanics and Physics of Solids 45, 21–50.
Ferracin, T., Landis, C.M., Delannay, F., Pardoen, T., 2003. On the determination of the cohesive zone properties of an adhesive layer from the analysis of the wedge-peel test. International Journal of Solids and Structures 40 (11), 2889–2904.
Gao, X., Kim, J., 2006. Modeling of ductile fracture: significance of void coalescence. International Journal of Solids and Structures 43, 6277–6293.

Garrison Jr., W.M., Moody, N.R., 1987. Ductile fracture. Journal of Physics and Chemistry of Solids 48, 1035–1074.

Giovanola, J.H., Cannizzaro, D., Doglione, R., Rossoll, A., 2006. Ductile fracture by void nucleation at tempering carbides. In: Gdoutos, E.E. (Ed.), Fracture of Nano and Engineering Materials and Structures. Springer.

Gologanu, M., Leblond, J.B., Perrin, G., Devaux, J., 1996. Recent extensions of Gurson's model for porous ductile metals. In: Sequet, P. (Ed.), Continuum Micromechanics. Springer-Verlag, pp. 61–130.

Hancock, J.W., Mackenzie, A.C., 1976. On the mechanisms of ductile failure in high-strength steels subjected to multi-axial stress-states. Journal of the Mechanics and Physics of Solids 24, 147–169.

Koplik, J., Needleman, A., 1988. Void growth and coalescence in porous plastic solids. International Journal of Solids and Structures 24, 835–853.

Leblond, J.B., Mottet, G., 2008. A theoretical approach of strain localization within thin planar bands in porous ductile materials. Comptes Rendus Mecanique 336 (1–2), 176–189.

Marciniak, K., Kuczynski, K., 1967. Limit strains in the process of stretch forming sheet metal. International Journal of Mechanical Sciences 9, 609–620.

McClintock, F.A., 1968. A criterion for ductile fracture growth of holes. Journal of Applied Mechanics 35, 363.

McVeigh, C., Vernerey, F., Liu, W., Moran, B., Olson, G., 2007. An interactive micro-void shear localization mechanism in high strength steels. Journal of Mechanics and Physics of Solids 55 (2), 225–244.

Mear, M.E., Hutchinson, J.W., 1985. Influence of yield surface curvature on flow localization in dilatant plasticity. Mechanics of Materials 4, 395–407.

Nahshon, K., Hutchinson, J.W., 2008. Modification of the Gurson model for shear failure. European Journal of Mechanics 27 (1), 1–17.

Needleman, A., Tvergaard, V., 1992. Analysis of plastic flow localization in metals. Applied Mechanics Reviews 45, S3–S18.

Pardoen, T., Hutchinson, J.W., 2000. An extended model for void growth and coalescence. Journal of Mechanics and Physics of Solids 48, 2467–2512.

Perrin, G., Leblond, J.B., 1993. Rudnicki and rice's analysis of strain localization revisited. Journal of Applied Mechanics 60, 842–846.

Pijnenburg, K.G.W., Van der Giessen, E., 2001. Macroscopic yield in cavitated polymer blends. International Journal of Solids and Structures 38, 3575–3598.

Rice, J.R., 1977. The localization of plastic deformation. In: Koiter, W.T. (Ed.), Theoretical and Applied Mechanics. North-Holland, pp. 207–220.

Rice, J.R., Tracey, D.M., 1969. On the ductile enlargement of voids in triaxial stress fields. Journal of the Mechanics and Physics of Solids 17, 201–217.

Rudnicki, J.W., Rice, J.R., 1975. Conditions for the localization of deformation in pressure-sensitive dilatant materials. Journal of the Mechanics and Physics of Solids 23, 371–394.

Saje, M., Pan, J., Needleman, A., 1982. Void nucleation effects on shear localization in porous solids. International Journal of Fracture 19, 163–182.

Scheyvaerts, F., Onck, P.R., Tekoglu, C., Pardoen, T., in press. The growth and coalescence of voids under combined shear and tension. Journal of the Mechanics and Physics of Solids, 2010. doi:10.1016/j.jmps.2010.10.003.

Scheyvaerts, F., Pardoen, T., Onckn, P.R., 2010. A new model for void coalescence by internal necking. International Journal of Damage Mechanics 19 (1), 95–126.

Siruguet, K., Leblond, J.B., 2004a. Effect of void locking by inclusions upon the plastic behavior of porous ductile solids – I: Theoretical modeling and numerical study of void growth. International Journal of Plasticity 20 (2), 225–254.

Siruguet, K., Leblond, J.B., 2004b. Effect of void locking by inclusions upon the plastic behavior of porous ductile solids – Part II: Theoretical modeling and numerical study of void coalescence. International Journal of Plasticity 20 (2), 255–268.

Thomason, P.F., 1985. Three-dimensional model for the plastic limit-load at incipient failure of the intervoid matrix in ductile porous solid. Acta Metallurgica 33, 1079–1085.

Tvergaard, V., 1981. Influence of voids on shear band instabilities under plane strain conditions. International Journal of Fracture 17, 389–407.

Tvergaard, V., 1982. Ductile fracture by cavity nucleation between larger voids. Journal of the Mechanics and Physics of Solids 30, 265–286.

Tvergaard, V., 1989. Numerical study of localization in a void-sheet. International Journal of Solids and Structures 25 (10), 1143–1156.

Tvergaard, V., 2009a. Behaviour of voids in a shear field. International Journal of Fracture 158, 41–49.

Tvergaard, V., 2009b. Shear deformation of voids with contact modelled by internal pressure. International Journal of Mechanical Sciences 50, 1459–1465.

Weck, A., Wilkinson, D.S., Toda, H., Marie, E., 2006. 2d and 3d visualization of ductile fracture. Advanced Engineering Materials 8 (6), 469–472.

Wierzbicki, T., Bao, Y., Lee, Y.W., Bai, Y., 2005. Calibration and evaluation of seven fracture models. International Journal of Mechanical Sciences 47, 719–743.

Yamamoto, H., 1978. Conditions for shear localization in the ductile fracture of void-containing materials. International Journal of Fracture 14, 347–365.

Zhang, K.S., Bai, J.B., Francois, D., 2001. Numerical analysis of the influence of the lode parameter on void growth. International Journal of Solids and Structures 38, 5847–5856.